PROCEEDINGS A

royalsocietypublishing.org/journal/rspa

Research

Cite this article: Lawrie JB, Nennig B, Perrey-Debain E. 2022 Analytic mode-matching for accurate handling of exceptional points in a lined acoustic waveguide. *Proc. R. Soc. A* **478**: 20220484. https://doi.org/10.1098/rspa.2022.0484

Received: 18 July 2022
Accepted: 18 November 2022

Subject Areas:
applied mathematics, acoustics, wave motion

Keywords:
exceptional point, complex symmetric operator, waveguide, mode-matching, point-wise convergence, transmission loss

Author for correspondence:
Jane B. Lawrie
e-mail: Jane.Lawrie@brunel.ac.uk

Analytic mode-matching for accurate handling of exceptional points in a lined acoustic waveguide

Jane B. Lawrie[1], B. Nennig[2] and E. Perrey-Debain[3]

[1]Department of Mathematics, Brunel University London, Uxbridge UB8 3PH, UK
[2]Institut Supérieur de Mécanique de Paris, (ISAE-SUPMECA)—Laboratoire Quartz EA 7393, 3 rue Fernand Hainaut, Saint-Ouen 93407, France
[3]Université de Technologie de Compiègne, Roberval (Mechanics, Energy and Electricity), Centre de Recherche Royallieu, CS 60319, Compiègne Cedex 60203, France

JBL, 0000-0003-3674-5605; BN, 0000-0002-0309-7165

Exceptional points (which occur when two or more modes coalesce) have long been associated with optimal attenuation in lined acoustic waveguides. In recent years, with a view to optimizing sound absorption, some effort has gone into designing liners that generate exceptional points (EPs) at specified frequencies. However, analytic modelling of acoustic scattering in the presence of an EP is not well developed, with most authors relying on standard methods applied close to (but not at) EP conditions. Indeed, exact treatment requires care since the mathematical system under-pinning the scattering process is degenerate. This article presents an analytic mode-matching approach to modelling the scattering of a plane wave travelling towards the junction of a rigid duct with a lined duct at EP conditions. Both EP2 and EP3 (coalescence of two and three modes respectively) are considered. The enhanced mode-matching scheme is shown to be valid and numerically robust, and it is anticipated that it will be straightforward to adapt to a wide range of applications involving complex symmetric operators.

THE ROYAL SOCIETY PUBLISHING

1. Introduction

Suppression of noise transmitted in ducts within, e.g. aero-engines, gas turbines, blowers and mufflers, is a topic of longstanding interest to scientists and engineers. A well-established approach is to add an absorbent coating or lining to the interior duct walls; this then leads to the question of how to develop the optimal lining for a particular application. In this quest Cremer's concept of optimal attenuation is of interest. In 1953, Cremer [1] showed that the optimum attenuation within a lined duct occurs when a mode pair degenerates into a single mode (i.e. when two eigenvalues and their corresponding eigenmodes merge). This phenomenon, commonly referred to as an *exceptional point* (EP2), is, of course, not confined to acoustic propagation in waveguides; it is ubiquitous in non-Hermitian waves physics (see [2–4] and the references therein).

Some 20 years after Cremer's work was published, Tester [5] derived the Green's function for a two-dimensional duct with an optimal impedance lining along one wall. He showed that numerical results for the attenuation compared favourably with experimental data. Further notable extensions from the same decade include the works by Zorumski and Mason [6] who extended Tester's analysis to circular ducts with locally reacting liners and Koch [7] who used a Wiener–Hopf approach to study acoustic power attenuation in a duct with multiple sections of lining. Cremer's concept received little further attention until quite recently when a number of papers exploring the idea in the context of noise attenuation within circular and/or annular ducts with flow [8–13] appeared in the literature. It is worth noting that EPs also occur in phenomena such as zeros in group velocity [14] or instability in, for example, thermoacoustics [15]. However, in all contexts, exact mathematical treatment requires some care since, close to the EP, the usual set of eigenmodes do not form a complete basis, and this is manifest as degeneracy in the mathematical system under-pinning the scattering process.

In the context of non-Hermitian physics, the EP degeneracy occurs most often in the scattering matrix and is associated with a number of unusual phenomena involving absorption (zeros) or lasing[1] (poles). For example, Feng *et al.* [16] realized unidirectional reflectionless light transport by constructing a planar, multilayered optical structure and modelling this as a two-port system, manipulating the elements of the scattering matrix to achieve an EP. Further insights into acoustic propagation at or near an EP are presented in [17–19] and, in particular, [20] discusses the form of the additional wavefunctions required at EP2 and EP3 (arising when three modes coalesce) to ensure completeness. These functions, analogous to Jordan generalized vectors in a finite-dimensional vector space, compensate for the loss of one or more dimensions in the space spanned by the natural eigenmodes. It is worth commenting that, at an EP, the additional wavefunctions introduce a linear (EP2) or quadratic (EP3) spatial growth [20–23], which moderates the exponential attenuation—although clearly this dominates at large distance from the source. This means that the attenuation depends not only on the source type but also on how it couples to the additional wavefunctions, as discussed in [19] for acoustic waveguides or in [24] for the photonic context.

Fundamental to the study of EPs is, of course, the ability to accurately locate the roots of a characteristic equation and the parameters leading to EP. To this end, two of the present authors have recently proposed a numerical algorithm which enables the trajectories of the eigenvalues in the vicinity of an exceptional point to be explored in a systematic way for discrete systems, such as those arising after the finite element discretization [25]. This work was followed by a comprehensive analysis of the behaviour of the transverse wavenumbers of a two-dimensional waveguide lined along both sides, as they coalesce in the vicinity of an optimal point [23]. In the latter article, numerical investigations suggest that the first EP3 (resulting from the coalescence of the first three modes) corresponds to maximum modal attenuation. Further, an expression for the Green's function, valid at EP2 and EP3, is presented.

[1]Krasnok *et al.* [2] explain that 'lasing occurs when a pole touches the real axis at the threshold value of gain, corresponding to an eigenvector of the scattering matrix with an infinite eigenvalue'.

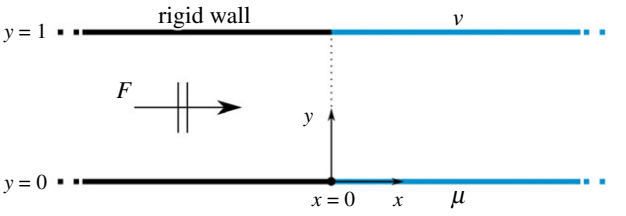

Figure 1. Diagram of the model problem. (Online version in colour.)

In this article, the authors consider a canonical problem involving acoustic wave propagation in a horizontal two-dimensional waveguide comprising two semi-infinite sections, which meet along a vertical interface. One duct has rigid boundaries, while the other is lined along both walls. (This geometry is not limited to acoustics, it can be found in other fields, e.g. in optics where waveguides with high-permittivity cladding have recently been studied [26].) A plane acoustic wave is incident along the rigid duct towards the interface, and the aim is to accurately determine the reflected and transmitted sound fields. For the case of no EP, the solution is presented using a standard analytic mode-matching scheme. The mode-matching scheme is then extended, by including additional waveforms, to the cases of EP2 and EP3. As far as the authors are aware, this is the first occasion that an analytic mode-matching procedure which is valid at EP conditions has appeared in the literature. A comprehensive discussion of the validity and convergence of the resulting numerical scheme is presented. This is followed by an investigation into the reflected and transmitted power focusing on three cases: the classical Tester's case (EP2) in which one wall is rigid, an EP3 arising for when both the wall parameters correspond to an absorbing lining and a specific scenario in which one wall is active and the other absorbing such that the wall parameters form a complex conjugate pair. In different contexts, the latter situation is typical of parity-time (PT) symmetric systems which have attracted significant interest in recent years [27–29]. Finally, the appendix presents new analytic results relating to the orthogonality properties of the additional eigenfunctions and point-wise convergence of the modal expansion at EP2.

2. The model problem

Consider a two-dimensional waveguide of height a comprising two semi-infinite sections (see figure 1), which meet along a vertical interface which, in a Cartesian frame of reference, is specified by $\hat{x} = 0$. The lower wall of the waveguide lies along $\hat{y} = 0$, $-\infty < \hat{x} < \infty$ and a compressible fluid of density ρ and sound speed c occupies the interior region of the duct. Under the assumption of harmonic time dependence, $\mathrm{e}^{-\mathrm{i}\omega\hat{t}}$, where $\omega = c\hat{k}$ is the radian frequency (in which $\hat{k}$ is the fluid wavenumber), the boundary value problem can be non-dimensionalized according to $\hat{x} = ax$, $\hat{y} = ay$ and $\omega\hat{t} = t$, the governing equation is then:

$$(\nabla^2 + k^2)\psi = 0, \tag{2.1}$$

where $k = \hat{k}a$ and $\psi(x, y)$ is the non-dimensional reduced (time independent) fluid velocity potential, which may be expressed as follows:

$$\psi(x, y) = \begin{cases} \psi_1(x, y), & x < 0,\ 0 \le y \le 1 \\ \psi_2(x, y), & x > 0,\ 0 \le y \le 1 \end{cases}. \tag{2.2}$$

The duct lying in the region $x < 0$ has rigid boundaries which is reflected in the boundary conditions

$$\partial_y \psi_1 = 0, \quad y = 0 \text{ and } 1, x < 0. \tag{2.3}$$

The travelling waveforms for this duct are well known and need not be discussed in detail here.

The duct lying in the region $x > 0$ is lined, and the local boundary conditions are as follows:

$$\partial_y \psi_2 = -\mu \psi_2 \quad \text{at } y = 0 \quad \text{and} \quad \partial_y \psi_2 = \nu \psi_2 \quad \text{at } y = 1, \tag{2.4}$$

where $\mu = ic\rho\hat{k}a/Z_\mu$, $\nu = ic\rho\hat{k}a/Z_\nu$ are the non-dimensionalized wall admittances in which Z_μ and Z_ν are the associated complex acoustic impedances. In the absence of any exceptional points, the wave functions that satisfy (2.1) and the first of the boundary conditions in (2.4) are separable and have the form $Y(s, y)\,\mathrm{e}^{\mathrm{i}sx}$, where

$$Y(s, y) = \cos(\alpha y) - \frac{\mu}{\alpha}\sin(\alpha y) \quad \text{with } \alpha = \sqrt{k^2 - s^2}. \tag{2.5}$$

On substituting this into the second of the boundary conditions in (2.4), it is seen that the axial wavenumbers must satisfy

$$(\nu Y - \partial_y Y)_{y=1}\,\mathrm{e}^{\mathrm{i}sx} = K(s)\,\mathrm{e}^{\mathrm{i}sx} = 0, \tag{2.6}$$

where

$$K(s) = q\cos\alpha + \left(\alpha - \frac{p}{\alpha}\right)\sin\alpha \quad \text{with } \alpha = \sqrt{k^2 - s^2}, \tag{2.7}$$

with $q = \mu + \nu$ and $p = \mu\nu$. Note that the characteristic function defined in (2.7) could be viewed as a function of α (which is a function of s). However, as the analysis unfolds, it is more convenient to treat it as a function of s. That said, (2.7) is used to determine the transverse wavenumbers α_n, $n = 1, 2, 3, \ldots$ which are ordered by increasing real part. Then, the axial wavenumbers are calculated through $s_n = \sqrt{k^2 - \alpha_n^2}$, $n = 1, 2, 3, \ldots$ and, if necessary, are re-numbered according to the convention of largest (positive) real value first and then, once all real values are exhausted, by increasing imaginary part.

It is instructive to anticipate the approximate form for the transverse wavenumbers for large mode order n. It can be easily shown that roots of the characteristic equation (2.7) are similar to that of a rigid walled waveguide ($\mu = \nu = 0$). In fact, it is found that

$$\alpha_n = n\pi\left[1 - \frac{q}{(n\pi)^2} + \frac{q^3/3 - q^2 - pq}{(n\pi)^4} + \mathcal{O}\left(\frac{1}{(n\pi)^6}\right)\right], \quad \text{as } n \to \infty, \tag{2.8}$$

which gives a good approximation for moderate values of p and q. Thus, in the low-frequency approximation, $s_n \approx in\pi$ and the modes are strongly evanescent. It is worth noting that equation (2.8) also indicates that for the case $\mu = \nu^*$ (where the * indicates the complex conjugate) the roots α_n are real as $n \to \infty$. This does not necessarily imply that all the roots are real and, with reference to equation (2.7), it is worthwhile noting that, when $\tan(\mu) \approx \tan(\nu) \approx \pm i$, two further roots may occur at $\alpha \approx \pm i\mu$ and $\alpha \approx \pm i\nu$ and these are necessarily complex if the wall parameters are complex.

An EP arises when there exists α_n such that $K(s_n) = K'(s_n) = 0$. At an EP the eigenfunctions $Y_n(y) = Y(s_n, y)$, $n = 1, 2, 3 \ldots$ no longer form a complete set, and this is indicative of the existence of further (non-separable) waveform. Following [20,23], the new wave function can be defined by differentiation with respect to s, that is:

$$\psi_{\mathrm{EP}2} = \partial_s(Y\,\mathrm{e}^{\mathrm{i}sx}) = (Y' + \mathrm{i}xY)\,\mathrm{e}^{\mathrm{i}sx} \tag{2.9}$$

with

$$Y' = \partial_s Y = \frac{sy\sin(\alpha y)}{\alpha} + \frac{s\mu y\cos(\alpha y)}{\alpha^2} - \frac{s\mu\sin(\alpha y)}{\alpha^3}, \tag{2.10}$$

and it is easy to see that

$$\partial_s\{(\nu Y - \partial_y Y)\,\mathrm{e}^{\mathrm{i}sx}\}_{y=1} = (\nu\psi_{\mathrm{EP}2} - \partial_y\psi_{\mathrm{EP}2})_{y=1} = (K' + \mathrm{i}xK)\,\mathrm{e}^{\mathrm{i}sx}. \tag{2.11}$$

Thus, a non-separable waveform exists if both $K = 0$ and $K' = \partial_s K = 0$.[2] There also exists the possibility of EP3 whereby $K = 0$, $K' = \partial_s K = 0$ and $K'' = \partial_s^2 K = 0$. This condition leads to the

[2]The existence of the new wave function could have been anticipated because in situations where $K' \approx 0$, modes are nearly coalescing, i.e. $s_1 \approx s_2$ and therefore $Y(s_2, y)\,\mathrm{e}^{\mathrm{i}s_2 x} - Y(s_1, y)\,\mathrm{e}^{\mathrm{i}s_1 x} \approx (s_2 - s_1)\psi_{\mathrm{EP}2}$.

Table 1. Numerical values (shown to five-digit accuracy) of the wall parameters giving rise to the EPs considered in §4.

EP type	upper wall	lower wall	transverse wavenumber
EP2	$\bar{\nu} = 1.6506 + 2.0599\mathrm{i}$	$\bar{\mu} = 0 + 0.\mathrm{i}$	$\bar{\alpha}_1 = 2.1061 - 1.1253\mathrm{i}$
EP3	$\bar{\bar{\nu}} = 3.1781 + 4.6751\mathrm{i}$	$\bar{\bar{\mu}} = 3.0875 + 3.6234\mathrm{i}$	$\bar{\bar{\alpha}}_1 = 4.1969 - 2.6086\mathrm{i}$
EP3-PT	$\bar{\bar{\nu}} = 1.0119 + 4.6029\mathrm{i}$	$\bar{\bar{\mu}} = 1.0119 - 4.6029\mathrm{i}$	$\bar{\bar{\alpha}}_1 = 4.6015$

existence of another wavefunction:

$$\psi_{\mathrm{EP3}} = \partial_s^2(Y\,\mathrm{e}^{\mathrm{i}sx}) = (Y'' + 2\mathrm{i}xY' - x^2Y)\,\mathrm{e}^{\mathrm{i}sx}. \tag{2.12}$$

The location of exceptional points in the complex plane has been discussed in the literature, and a thorough description can be found in the recent paper [23] by the present authors. The reader is reminded that EP2s form a continuum [23]. That is, to a given arbitrary complex-valued transverse wavenumber $\bar{\alpha}$, there corresponds a unique pair of wall parameters obtained from

$$\bar{\mu}\bar{\nu} = \bar{\alpha}^2\left(\frac{2\bar{\alpha} + \sin(2\bar{\alpha})}{2\bar{\alpha} - \sin(2\bar{\alpha})}\right) \quad \text{and} \quad \bar{\mu} + \bar{\nu} = -\left(\bar{\alpha} - \frac{\bar{\mu}\bar{\nu}}{\bar{\alpha}}\right)\tan\bar{\alpha}, \tag{2.13}$$

where, following the notation of [23], the overbars indicate that these are EP2 values of the parameters (i.e. the overbar does not indicate the complex conjugate). On the other hand, EP3s admit only discrete values of the transverse wavenumber which, on denoting these by a double overbar, are the solutions [7] to:

$$4\cos\bar{\bar{\alpha}} - \frac{\sin\bar{\bar{\alpha}}}{\bar{\bar{\alpha}}^2}(2\bar{\bar{\alpha}} + \sin(2\bar{\bar{\alpha}})) = 0. \tag{2.14}$$

The corresponding wall parameters are found using (2.13), and the exact relationship $\bar{\bar{\alpha}}^4 = \bar{\bar{\nu}}^2\bar{\bar{\mu}}^2 - \bar{\bar{\nu}}\bar{\bar{\mu}}(\bar{\bar{\nu}} + \bar{\bar{\mu}})$ is worth noting. It is also worth commenting that, for fixed k, higher order EPs do not exist for this geometry because there are only two complex parameters.

The exceptional points that are of interest in this article correspond to the coalescence of the first two (EP2) or three (EP3) modes and are reported in table 1. The first line corresponds to the now famous Tester's case (EP2) with one rigid wall and the second line shows that EP3 can exist by careful choice of the wall parameters (here both absorbing). Note, however, that EPs are not necessarily associated with absorbing boundary conditions in which the imaginary part of the wall parameters (or equivalently the real part of the walls impedance) must be positive. Active walls can also give rise to exceptional points [26]. The last line of table 1 refers to a specific scenario in which one wall is active and the other absorbing such that the wall parameters are complex conjugates. This situation is typical of PT-symmetric systems which have attracted intensive research interest in recent years. Figure 2 shows the location in the complex α-plane of the transverse wavenumbers at EP conditions.

To complete the discussion of the formation and significance of EPs it is useful to recollect that EPs are associated with the coalescence of $r = 2$ or 3 modes. In fact, a slight perturbation of the upper wall parameter $\nu = \bar{\nu} + \delta$ (while the lower wall admittance is kept constant) permits separation of the EP into the r associated classical roots of the characteristic equation, and it can be shown that [23]

$$\alpha_n = \alpha_{\mathrm{EP}} + z^n\delta^{1/r}(-r!\partial_\alpha^r K)^{1/r} + \mathcal{O}(\delta^{2/r}), \quad n = 1, \ldots, r, \tag{2.15}$$

where partial derivatives must be evaluated at the EP, i.e. at $\alpha_{\mathrm{EP}} = \bar{\alpha}_1 (r = 2)$ or $\alpha_{\mathrm{EP}} = \bar{\bar{\alpha}}_1 (r = 3)$ and z is the rth root of unity, $z^r = 1$. Equation (2.15) implies that roots are very sensitive in the vicinity of EPs, and this augments with r. Note that the case of the EP3-PT is particularly impacted by (2.15) since separated roots necessarily lie on both sides of the complex plane leading to both attenuated and amplified waves.

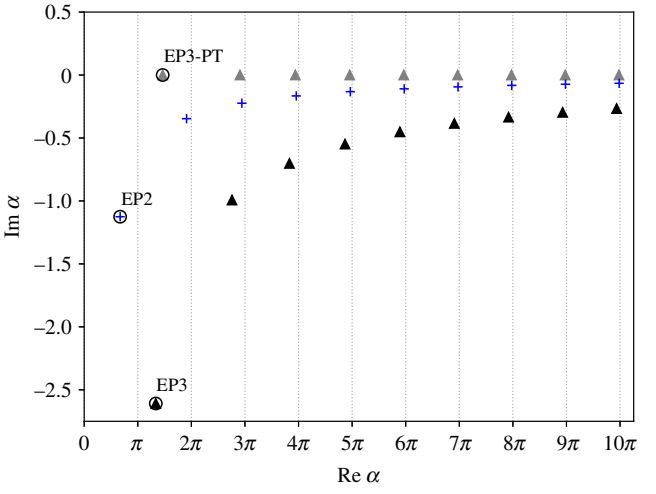

Figure 2. Location of the roots of $K = 0$ in the complex α-plane using the parameters of table 1. For each family of roots, the first (indicated with a circle) corresponds to the EP listed in table 1. (Online version in colour.)

3. The mode-matching solution

The mode-matching method is a convenient tool by which to solve boundary problems of the type outlined in §2. In the absence of an exceptional point, the method is well established and known to be of good accuracy. To be precise, provided sufficient terms are taken, the pressure and mean velocity are guaranteed to agree with a high level of accuracy at the matching interface, whereas the agreement between the normal velocities depends on the strength of the singularity in the velocity field, see, e.g. [30,31]. As far as the authors are aware, a valid analytic mode-matching procedure has not appeared in the literature for EP conditions, and one of the main purposes of this article is to extend the method to these situations. Thus, three cases will be considered: no EP, EP2 and EP3. Attention will be restricted to the case where the EP occurs in α_1 which corresponds to the axial wavenumber with the smallest imaginary part, s_1. Henceforth, an overbar will be used to denote those modal coefficients arising from terms associated with EP2 and a double overbar in the case of EP3. However, for the sake of simplicity of notation, the wall parameters and wavenumbers will not be barred as the nature of the EP will be clear from the context.

In all three cases, the velocity potentials can be expressed as eigenfunction expansions (although the form of this expansion varies for the duct lying in $x > 0$). For the inlet duct, the expansion has the form:

$$\psi_1 = F\,\mathrm{e}^{\mathrm{i}kx} + \sum_{n=0}^{\infty} A_n \cos(n\pi y)\,\mathrm{e}^{-\mathrm{i}\eta_n x}, \quad x < 0, \tag{3.1}$$

where the coefficient A_n is the complex amplitude of nth reflected mode. The first term in (3.1) is a plane incident wave of amplitude F and the non-dimensional axial wavenumbers are defined by $\eta_n = \sqrt{k^2 - n^2\pi^2}$, $n = 0, 1, 2, \ldots$. Note that this eigenfunction expansion reduces to a standard Fourier cosine series at $x = 0$.

(a) Standard mode-matching: no EP

In the absence of an EP, the velocity potential for the duct lying in the region $x > 0$ has the form:

$$\psi_2 = \sum_{n=1}^{\infty} B_n Y_n(y)\,\mathrm{e}^{\mathrm{i}s_n x}, \quad x > 0, \tag{3.2}$$

where the coefficient B_n is the complex amplitude of nth transmitted mode. The eigenfunctions $Y_n(y) = Y(s_n, y)$, $n = 1, 2, 3, \ldots$ satisfy the orthogonality relation

$$\int_0^1 Y_m(y) Y_n(y)\, \mathrm{d}y = \delta_{mn} P_n, \tag{3.3}$$

where δ_{mn} is the Kronecker delta and the quantity P_n is defined by

$$P_n = \int_0^1 Y_n^2(y)\, \mathrm{d}y = -\frac{Y_n(1)}{2s_n} K'(s_n). \tag{3.4}$$

The right-hand side of (3.4) is obtained following Lawrie's work [32,33], and further details are given in the appendix.

The modal coefficients A_n, $n = 0, 1, 2, \ldots$ and B_n, $n = 1, 2, 3, \ldots$ are determined by imposing continuity of pressure ($\psi_1(0, y) = \psi_2(0, y)$) and normal velocity ($\partial_x \psi_1(0, y) = \partial_x \psi_2(0, y)$) at the matching interface ($x = 0$, $0 \le y \le 1$). On multiplying through by $\cos(m\pi y)$ and using the standard orthogonality condition for cosine to isolate the coefficients A_m, continuity of pressure yields:

$$A_m = -\frac{2F}{\epsilon_m}\delta_{m0} + \frac{2}{\epsilon_m}\sum_{n=1}^{\infty} B_n L_{mn}, \tag{3.5}$$

where $\epsilon_n = 2$ if $n = 0$ and 1 otherwise, and

$$L_{mn} = \int_0^1 Y_n(y) \cos(m\pi y)\, \mathrm{d}y. \tag{3.6}$$

Similarly, on multiplying through by $Y_j(y)$, (3.3) can be applied to isolate the coefficients B_j via the normal velocity condition:

$$B_j = \frac{kF}{s_j P_j} L_{0j} - \frac{1}{s_j P_j}\sum_{n=0}^{\infty} A_n \eta_n L_{nj}, \quad j \ge 1. \tag{3.7}$$

The modal coefficients are now obtained by truncating (3.5) and (3.7) and numerically solving the resulting finite algebraic system.

It is worth noting that, for the lined duct ($x > 0$), Helmholtz's equation together with the impedance boundary conditions comprise a complex symmetric operator for the duct modes. This property is manifest in the 'scattering matrix' and is apparent on combining equations (3.5) and (3.7) as follows:

$$b_j = \frac{2kF}{\sqrt{s_j P_j}} L_{0j} - 2\sum_{n=0}^{\infty} b_n \mathcal{S}_{jn}, \quad j \ge 1, \tag{3.8}$$

where

$$\mathcal{S}_{jn} = \frac{1}{\sqrt{s_j s_n P_j P_n}}\sum_{m=0}^{\infty} \frac{\eta_m}{\varepsilon_m} L_{mj} L_{mn} \tag{3.9}$$

and $b_n = B_n\sqrt{s_n P_n}$, $n = 1, 2, 3, \ldots$.

(b) Enhanced mode-matching: EP2

At EP2 conditions, α_1 is a double root of $K(s) = 0$, and since $K'(s_1) = 0$ which implies that $P_1 = 0$, $Y_1(y)$ is self-orthogonal and the system of equations given in (3.5) and (3.7) is degenerate. An extra function is now required to correctly represent the transmitted wave field. As mentioned in §2 (see (2.9)), the additional waveform is the derivative of $Y(s, y)\, \mathrm{e}^{\mathrm{i}sx}$ with respect to s. However, to ensure the simplest structure for the EP2 eigenfunction expansion, it is convenient to re-express this waveform in terms of functions of y and derivatives with respect to y. This is done by noting

that:

$$\partial_s Y|_{s=s_1} = -\frac{s_1}{\alpha_1^2}\chi(y) + \frac{s_1\mu^2}{\alpha_1^2(\alpha_1^2+\mu^2)}Y_1(y), \tag{3.10}$$

where

$$\chi(y) = \left(y - \frac{\mu}{\alpha_1^2+\mu^2}\right)\partial_y Y_1. \tag{3.11}$$

On considering (2.9) and (3.10), it is clear that only the functions $\chi(y)\,\mathrm{e}^{\mathrm{i}s_1 x}$ and $\mathrm{i}xY_1(y)\,\mathrm{e}^{\mathrm{i}s_1 x}$ need to be added to the eigenfunction expansion for ψ_2 because the term of (3.10) involving $Y_1(y)$ can be incorporated into the sum of the usual separable modes. Thus, at EP2 conditions, the enhanced eigenfunction expansion for ψ_2 takes the form:

$$\psi_2 = \bar{B}_1\left\{\frac{s_1}{\alpha_1^2}\chi(y) - \mathrm{i}xY_1(y)\right\}\mathrm{e}^{\mathrm{i}s_1 x} + \sum_{n=1}^{\infty} B_n Y_n(y)\,\mathrm{e}^{\mathrm{i}s_n x}, \quad x>0, \tag{3.12}$$

where the coefficient $\bar{B}_1$ is associated with the additional functions and the overbar indicates that these occur due to the double root α_1. It is important to note that the function $\chi(y)$ is needed to ensure that the eigenfunction expansion (3.12) converges point-wise to ψ_2 and also that $\chi(y)$ satisfies the following orthogonality property (see appendix for verification of these points):

$$\int_0^1 \chi(y)Y_n(y)\,\mathrm{d}y = Q\delta_{1n} \quad \text{where } Q = \frac{\alpha_1^2}{4s_1^2}Y_1(1)K''(s_1). \tag{3.13}$$

It is further worth noting that $Q=0$ at EP3.

In this case, continuity of pressure yields:

$$A_m = -\frac{2F}{\epsilon_m}\delta_{m0} + \frac{2s_1}{\epsilon_m\alpha_1^2}\bar{B}_1 M_m + \frac{2}{\epsilon_m}\sum_{n=1}^{\infty} B_n L_{mn}, \tag{3.14}$$

where

$$M_m = \int_0^1 \chi(y)\cos(m\pi y)\,\mathrm{d}y, \tag{3.15}$$

while continuity of normal velocity gives:

$$B_j = \frac{kF}{s_j P_j}L_{0j} - \frac{1}{s_j P_j}\sum_{n=0}^{\infty} A_n\eta_n L_{nj}, \quad j>1. \tag{3.16}$$

Note that, since $Y_1(y)$ is self-orthogonal, (3.16) is valid only for $j>1$. However, although it yields no information about B_1, (3.3) does provide information about $\bar{B}_1$ and use of (3.13) provides a further equation. Thus, there are two additional equations for B_1 and $\bar{B}_1$:

$$\begin{pmatrix} s_1 Q & \frac{s_1^2}{\alpha_1^2}T - Q \\ 0 & \frac{s_1^2}{\alpha_1^2}Q \end{pmatrix}\begin{pmatrix} B_1 \\ \bar{B}_1 \end{pmatrix} = \begin{pmatrix} kFM_0 - \sum_{n=0}^{\infty} A_n\eta_n M_n \\ kFL_{01} - \sum_{n=0}^{\infty} A_n\eta_n L_{n1} \end{pmatrix}, \tag{3.17}$$

where

$$T = \int_0^1 \chi^2(y)\,\mathrm{d}y. \tag{3.18}$$

The coefficients A_n, $n=0,1,2,\ldots$, $\bar{B}_1$ and B_n, $n=1,2,3,\ldots$ are now obtained by truncating (3.14) and (3.16) and numerically solving the resulting finite algebraic system together with (3.17).

(c) Enhanced mode-matching: EP3

At EP3 conditions, α_1 is a triple root of $K(s)=0$. In this case, not only is $Y_1(y)$ self-orthogonal but also $\chi(y)$ is orthogonal to $Y_1(y)$, i.e. $P_1 = Q = 0$. It follows that the determinant of the matrix on the left-hand side of (3.17) is zero and the system is degenerate. A further function is thus required

to accurately represent ψ_2 as an eigenfunction expansion, and this is related to the additional waveform defined in (2.12). A little manipulation gives:

$$\partial_s^2 Y|_{s=s_1} = -\frac{s_1^2}{\alpha_1^2}\xi(y) + \Upsilon(s_1)\chi(y) + CY_1(y), \tag{3.19}$$

where

$$\xi(y) = \left(y - \frac{\mu}{\alpha_1^2+\mu^2}\right)^2 Y_1(y) - \frac{2\mu}{(\alpha_1^2+\mu^2)^2}\partial_y Y_1 \tag{3.20}$$

and

$$\Upsilon(s) = \frac{2s^2}{\alpha^2(\alpha^2+\mu^2)} - \frac{\alpha^2+3s^2}{\alpha^4}. \tag{3.21}$$

The quantity C of (3.19) is independent of y, and its exact definition is not necessary for the purposes of this article because this term can be incorporated into the sum of the usual separable modes. Thus, on considering (2.12) and (3.19), at EP3 conditions, the enhanced eigenfunction expansion for ψ_2 takes the form:

$$\begin{aligned}\psi_2 = \bar{\bar{B}}_1 &\left\{-\frac{s_1^2}{\alpha_1^2}\xi(y) + \Upsilon(s_1)\chi(y) - 2\mathrm{i}x\left(\frac{s_1}{\alpha_1^2}\chi(y) - \frac{s_1\mu^2 Y_1(y)}{\alpha_1^2(\alpha_1^2+\mu^2)}\right) - x^2 Y_1(y)\right\}\mathrm{e}^{\mathrm{i}s_1 x}\\ &+ \bar{B}_1\left\{\frac{s_1}{\alpha_1^2}\chi(y) - \mathrm{i}xY_1(y)\right\}\mathrm{e}^{\mathrm{i}s_1 x} + \sum_{n=1}^{\infty} B_n Y_n(y)\,\mathrm{e}^{\mathrm{i}s_n x}, \quad x>0,\end{aligned} \tag{3.22}$$

where the coefficient $\bar{\bar{B}}_1$ is associated with the new additional functions and the double overbar is used to indicate that these occur due to the triple root α_1. Note that $\xi(y)$ has the following orthogonality property:

$$\int_0^1 \xi(y)Y_n(y)\,\mathrm{d}y = R\delta_{1n} \quad \text{where } R = \frac{\alpha_1^2}{6s_1^3}Y_1(1)K'''(s_1). \tag{3.23}$$

Continuity of pressure now yields:

$$A_m = -\frac{2F}{\epsilon_m}\delta_{m0} + \frac{2}{\epsilon_m}\bar{\bar{B}}_1\left\{-\frac{s_1^2}{\alpha_1^2}N_m + \Upsilon(s_1)M_m\right\} + \frac{2s_1}{\epsilon_m\alpha_1^2}\bar{B}_1 M_m + \frac{2}{\epsilon_m}\sum_{n=1}^{\infty} B_n L_{mn}, \tag{3.24}$$

where

$$N_m = \int_0^1 \xi(y)\cos(m\pi y)\,\mathrm{d}y, \tag{3.25}$$

while continuity of normal velocity gives:

$$B_j = \frac{kF}{s_j P_j}L_{0j} - \frac{1}{s_j P_j}\sum_{n=0}^{\infty} A_n\eta_n L_{nj}, \quad j>1, \tag{3.26}$$

where again this is valid only for $j>1$. For $j=1$, an expression containing only $\bar{\bar{B}}_1$ (and the coefficients A_n) is obtained using (3.3). Two further equations are obtained using (3.13) and (3.23). Thus,

$$\begin{pmatrix} s_1R & \frac{s_1^2}{\alpha_1^2}U - R & \Theta \\ 0 & \frac{s_1^2}{\alpha_1^2}T & \Omega \\ 0 & 0 & -\frac{s_1^3}{\alpha_1^2}R \end{pmatrix}\begin{pmatrix} B_1 \\ \bar{B}_1 \\ \bar{\bar{B}}_1 \end{pmatrix} = \begin{pmatrix} kFN_0 - \sum_{n=0}^{\infty} A_n\eta_n N_n \\ kFM_0 - \sum_{n=0}^{\infty} A_n\eta_n M_n \\ kFL_{01} - \sum_{n=0}^{\infty} A_n\eta_n L_{n1} \end{pmatrix}, \tag{3.27}$$

where

$$\Theta = s_1\Upsilon(s_1)U - \frac{2s_1}{\alpha_1^2}U - \frac{s_1^3}{\alpha_1^2}W + \frac{2\mu^2 s_1 R}{\alpha_1^2(\alpha_1^2+\mu^2)} \tag{3.28}$$

and

$$\Omega = s_1\Upsilon(s_1)T - \frac{2s_1}{\alpha_1^2}T - \frac{s_1^3}{\alpha_1^2}U \tag{3.29}$$

with

$$U = \int_0^1 \xi(y)\chi(y)\,\mathrm{d}y \quad \text{and} \quad W = \int_0^1 \xi^2(y)\,\mathrm{d}y.$$

The coefficients A_n, $n = 0, 1, 2, \ldots$, $\bar{B}_1$, $\bar{\bar{B}}_1$ and B_n, $n = 1, 2, 3, \ldots$ are now obtained by truncating (3.24) and (3.26) and numerically solving the resulting finite algebraic system together with (3.27).

4. Numerical results

This section is divided into two subsections. The first deals with the validity and convergence of the enhanced mode-matching method, while the second presents a comprehensive investigation of the transmission loss/transmitted power at EP conditions for the model problem considered herein. Throughout, the amplitude of the plane wave forcing term is chosen to be $F = 1/\sqrt{k}$, thereby ensuring unit input power for all frequencies. The expression used for non-dimensional power is

$$\mathcal{P}_j = \int_0^1 \mathrm{Im}\left(\psi_j^* \frac{\partial \psi_j}{\partial x}\right)\mathrm{d}y, \quad j = 1, 2, \tag{4.1}$$

where * denotes the complex conjugate. It is worth noting that, for ψ_1, this reduces to the usual form:

$$\mathcal{P}_1 = 1 - \mathcal{R} = 1 - \mathrm{Re}\sum_{n=0}^{\infty}\eta_n|A_n|^2, \tag{4.2}$$

where $\mathcal{R}$ is the reflected power, whereas, due to the lack of orthogonality between $Y_n(y)$ and $Y_n^*(y)$, $n = 1, 2, 3, \ldots$, $\mathcal{P}_2$ is best calculated using the integral as defined in (4.1). Note that the quantity $\mathcal{P}_2$, i.e. the transmitted power $\mathcal{T}$, is a function of x (with $x \geq 0$) and a power balance tells us that:

$$1 = \mathcal{P}_2(x) + \mathcal{R} + \int_0^x \mathrm{Im}(\mu|\psi_2(x', 0)|^2 + \nu|\psi_2(x', 1)|^2)\,\mathrm{d}x', \tag{4.3}$$

where the integral term accounts for the energy loss (or gain) at the walls.

(a) Validity and convergence of the method

Transmission loss,

$$\mathrm{TL} = -10\log_{10}\mathcal{T} \tag{4.4}$$

is a quantity that is of significant interest to engineers and generally their aim is to minimize this while simultaneously restricting the reflected power. It is presented here, however, as not only for its intrinsic value but also as a means to demonstrate the failure of the standard mode-matching method as an EP is encountered during a standard frequency sweep. In figures 3 and 4, the reflected power and TL are plotted against the non-dimensionalized acoustic wavenumber k for $x = 1$ and $x = 5$. The wall parameters μ and ν are modelled using the single degree-of-freedom (SDOF) mass-spring-damper model and are tuned to coincide with the absorbing EP3 (second row of table 1) and Tester's EP2 values, respectively, when $k = 1$. To be precise,

$$\mu(k) = \frac{\mathrm{i}k^2}{R_\mu k + \mathrm{i}b_\mu - \mathrm{i}d_\mu k^2} \quad \text{and} \quad \nu(k) = \frac{\mathrm{i}k^2}{R_\nu k + \mathrm{i}b_\nu - \mathrm{i}d_\nu k^2}$$

and where the real parameters R_μ, R_ν, b_μ, b_ν and d_μ, d_ν are chosen so that the appropriate EP is realized when $k = 1$ (see table 2).

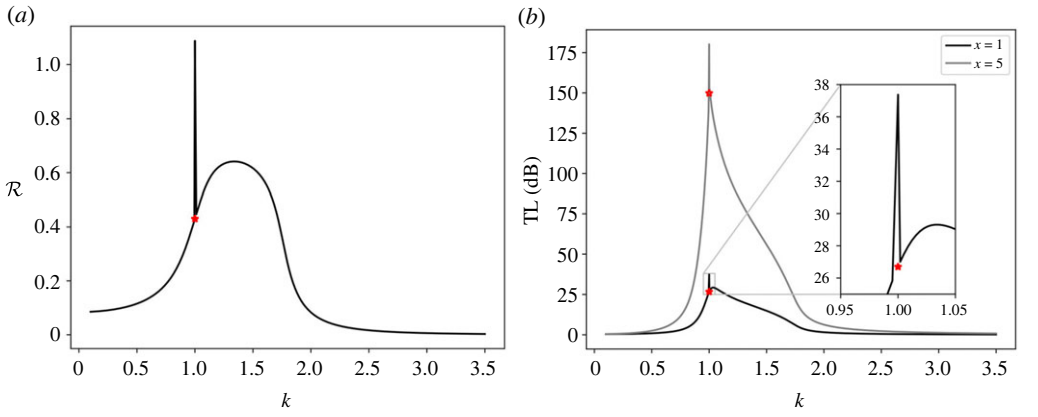

Figure 3. The (*a*) reflected power and (*b*) transmission loss at $x = 1$ and $x = 5$ for a SDOF liner. The spikes are erroneous and the stars indicate the correct values obtained using the enhanced matching scheme at the EP3. (Online version in colour.)

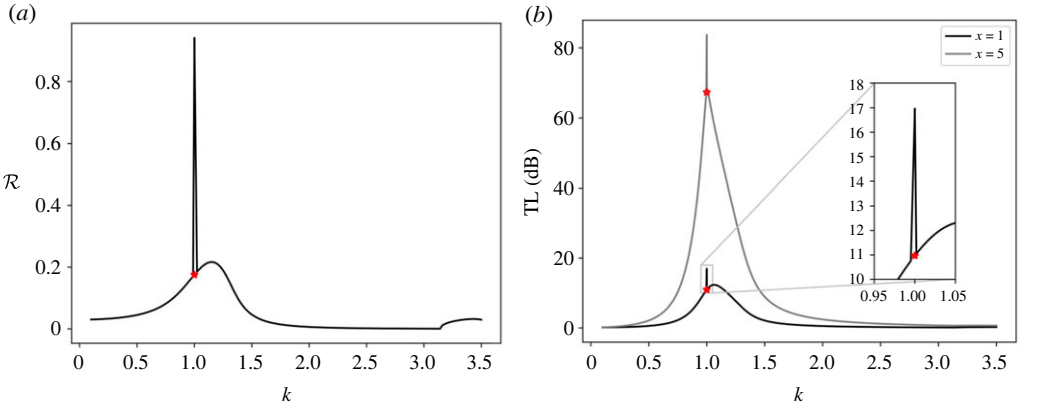

Figure 4. The (*a*) reflected power and (*b*) transmission loss at $x = 1$ and $x = 5$ for a SDOF liner. The spikes are erroneous and the stars indicate the correct values obtained using the enhanced matching scheme at Tester's EP2. (Online version in colour.)

Table 2. The numerical values used in the SDOF model.

EP2 ($\mu = 0$)			
$\nu(1) = \bar{\nu}$	$R_\nu = 0.2956$	$b_\nu = 0.9868$	$d_\nu = 0.75$
EP3			
$\mu(1) = \bar{\bar{\mu}}$	$R_\mu = 0.1598$	$b_\mu = 0.8862$	$d_\mu = 0.75$
$\nu(1) = \bar{\bar{\nu}}$	$R_\nu = 0.1463$	$b_\nu = 0.8494$	$d_\nu = 0.75$

This simple model yields a good local approximation for the liners traditionally used in aircraft engines, although the parameters used here are not chosen for their practical relevance. It is worth noting, however, that all the parameters are real valued meaning that tuning a liner on an EP3 can, in principle, be achieved. The results presented in figures 3 and 4 suggest that the TL is maximized at the EP values provided x is sufficiently large, and it is clear that, for parameters considered here, EP3 (figure 3) produces far better TL than Tester's EP2 (figure 4). The standard mode-matching procedure breaks down close to the EP (producing an erroneous spike on the otherwise smooth

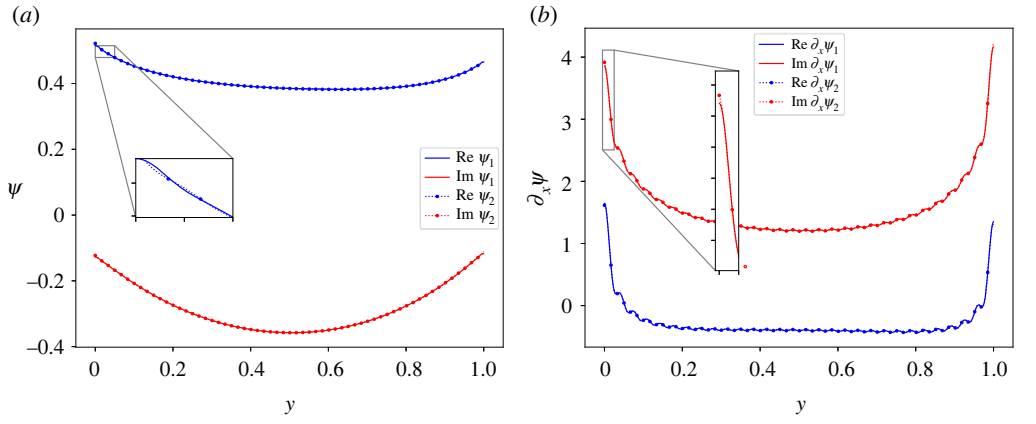

Figure 5. Validation of the matching conditions by comparing the real (blue) and imaginary part (red) of the potential and velocity field at the interface (with $k = 1$, $N = 60$) at EP3 conditions. The inset shows 'close up' near the lined wall. (*a*) ψ_i (upper curves [blue] are the real components) and (*b*) $\partial_x\psi_i$ (lower curves [blue] are the real components). (Online version in colour.)

curve). In fact, in these figures, the standard mode-matching procedure fails when $|k-1| < 10^{-5}$. The enhanced mode-matching for EP2 and EP3 has been used to calculate the correct values at the points of failure, and these are shown as stars. Although it might be expected that an EP would lead to some sort of singular behaviour, it is clear that this is not the case: the additional wavefuctions have regularized the mode-matching method and all components of the power are smooth functions of k at the EPs.

A fundamental assumption when implementing a mode-matching scheme is that the solution it generates corresponds to the solution to the physical problem in question. This article has presented a modified mode-matching scheme which enables a solution to be constructed at an EP and validation is necessary. In the appendix, it is proved that the modified modal expansion for EP2 converges point-wise to the intended function. However, the equivalent proof is not presented for EP3. The stars, calculated using the EP3 enhanced mode-matching method and superimposed on figure 3, do suggest that the method is correct but are not, in themselves, sufficient to validate the approach. With this in mind, it is now demonstrated that the matching conditions are indeed met by the solution obtained through the EP3 enhanced matching scheme. To this end, figure 5 shows the potential and the normal velocity (or equivalently the x-derivative of the potential) at the matching interface ($x = 0$) recovered from the modal expansions for domains 1 ($x < 0$) and 2 ($x > 0$). Here, $k = 1$ and, as for figure 3, the case of the EP3 with absorbing walls is considered. It is clear that the potential and the normal velocities for domains 1 ($x < 0$) and 2 ($x > 0$) are in good agreement at $x = 0$. The velocity field, computed with $N = 60$ modes, exhibits some ripples, which is characteristic of a Gibbs phenomenon. These oscillations could be smoothed using Lanczos-type filters [30,31] with no noticeable effect on the error. Further, the behaviour of the velocity near the wall suggests a logarithmic singularity which is in line with theoretical developments [34].

Having verified that the new approach produces the expected values for the transmission loss and that the matching conditions are met for EP3, the remainder of this section deals with the accuracy of the scheme. The following L^2 error is introduced:

$$\mathcal{E}_N^{\theta} = \frac{\sqrt{\int_0^1 |\theta_1(0,y) - \theta_2(0,y)|^2 dy}}{\sqrt{\int_0^1 |\theta_1(0,y)|^2 \, \mathrm{d}y}}, \tag{4.5}$$

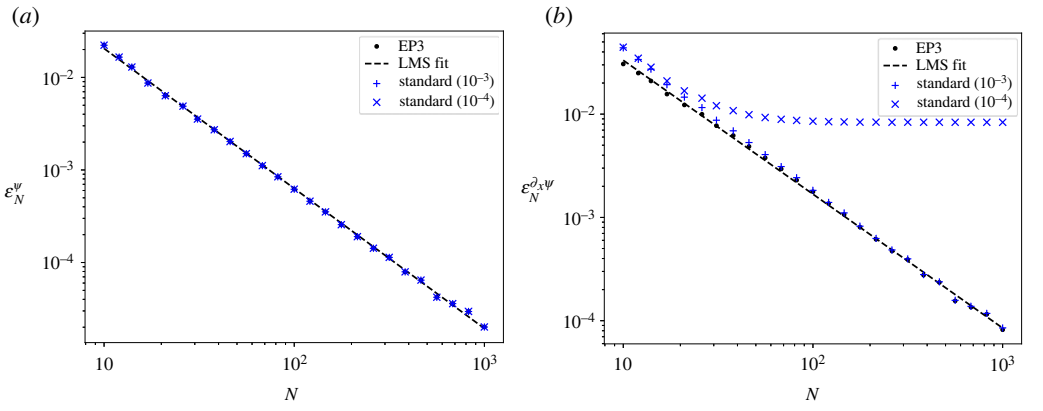

Figure 6. The error at the interface (logarithmic scale) against the number of modes N of the truncated series. The markers are data, and the dashed line is the least mean square fit with the ansatz $\mathcal{E}(N) = C/N^p$. The black bullet points are the exact matching scheme with additional wave functions, and the blue plus or cross markers are the standard matching scheme where both admittance values have been shifted a distance of $\delta = 10^{-3}$ or $\delta = 10^{-4}$, respectively, from the EP value. (*a*) Interface error for ψ and (*b*) interface error for $\partial_x\psi$. (Online version in colour.)

where function θ_j represents the truncated modal series (with N modes) for either the potential or its derivative in the x-direction, i.e. $\theta_j = \psi_j$ or $\partial_x\psi_j$, $j = 1, 2$. As this work focuses on coalescing (or nearly coalescing) modes, roots of the characteristic equation have to be computed carefully with appropriate solvers. In the present work, the first 10 modes (and their multiplicities) are obtained using the contour integral solver `POLZE` [35] based on the work developed in [36]. This approach offers the advantage that it does not require initial guesses and delivers very accurate results (up to about 10 digits of accuracy if necessary) even for multiple roots. Other roots, which are simple roots, are obtained using the asymptotic expression (2.8) for the initial guess and their accuracy is enhanced using Newton–Raphson iterations. All integrals arising from the continuity conditions are computed analytically. The interested reader can download the available open source software, see [37], that implements all aspects of the proposed method.

The convergence of the method with respect to the number of modes is shown in figure 6. It is observed, at least numerically, that the matching error at the interface as defined in (4.5) converges like

$$\mathcal{E}_N^{\theta} \sim N^{-p}. \tag{4.6}$$

In fact, by studying many test configurations with different values for the wall admittances (not necessarily associated with EPs), it is found that $p \approx 3/2$ for the velocity potential. To the authors' knowledge, a rigorous analysis of the convergence of the modal series at the interface is not well documented. However, in a somewhat different context, a similar power law, i.e. with $p = 3/2$, can be found in [38] for iris-type discontinuity problems in waveguides and periodic structures, and also in more recent papers [39,40] for duct acoustics with liners using rigid duct modified basis. Figure 6 shows the convergence of the method for three cases: the first (denoted by black bullet points) corresponds to the exact EP3 solution (absorbing walls) calculated at $k = 1$ using the additional wavefunctions in the modal series (see (3.22)). The other two curves (blue plus and cross markers) correspond to 'nearly EP3' configurations in which a slight modification has been made to both wall admittances, such that $\nu = \bar{\nu}(1 - \delta)$ and $\mu = \bar{\mu}(1 - \delta)$ with $\delta = 10^{-3}$ and $\delta = 10^{-4}$. For these, the standard mode-matching method is used (see (3.2)). Note that the convergence of the potential is not affected by moving slightly away from EP3. This, however, is not the case for the velocity. In this case, when the deviation from EP3 is too small (i.e. 10^{-4}), the error is slightly larger (than for 10^{-3}) for a low number of modes and the convergence

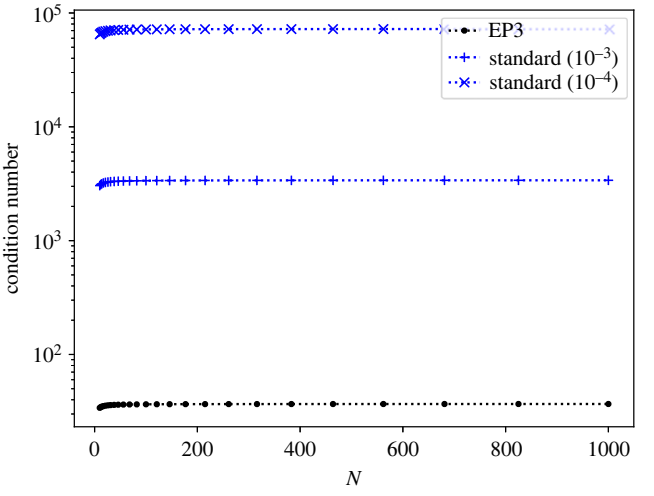

Figure 7. The condition number of the linear system (logarithmic scale) against the number of modes N. The black curve (bullet points) is the enhanced matching scheme with the additional wave functions, the blue ones (plus or cross markers) are the standard matching scheme where both wall admittances have been shifted a distance of $\delta = 10^{-3}$ or $\delta = 10^{-4}$, respectively, from the EP value. (Online version in colour.)

subsequently plateaus regardless of the number of modes. There are two reasons for this. First, when there are modes that are nearly coalescing the 'no-EP' algebraic system (equations (3.5)–(3.7)) is ill conditioned even for a small number of modes, see figure 7. This is a reflection of the fact that the nearly merging modes become almost self-orthogonal (see (3.4)) and P_j tends to 0 in (3.7) for these modes. Second, the convergence will be driven by the ability of the root finding method to handle multiple or clustered roots since the additional waveforms are in this case implicitly constructed from genuine modes. In practice, the threshold for δ will depend on the root finding method and tuning. In contrast, for the enhanced mode-matching, the condition number (calculated using the standard 2-norm) remains below 50, indicating good numerical stability for the modified approach (tested up to $N = 1000$). These results confirm that the standard mode-matching method may fail or become numerically unstable in the vicinity of an EP, especially for finite-sized problems where the condition number may also be altered by evanescent waves [41].

(b) Transmitted power

The results presented in this subsection focus on the power transmission (energy flux) along the lined duct as a function of x at three (or four) distinct frequencies at both EP2 and EP3. The parameters μ and ν are selected from the three cases reported in table 1. In figure 8, the transmitted power $\mathcal{T}$ as defined in (4.1) is plotted on a logarithmic scale against distance along the waveguide x for $k = 1, 10, 30$ at (a) EP2 and (b) EP3. For figure 8*a*, the values of the wall parameters are chosen from the first line of table 1, which corresponds to Tester's case (EP2 with one rigid wall), while for figure 8*b*, the parameters are chosen from the second line of table 1 (the absorbing EP3). Also plotted (the dotted lines) is the power associated with usual separable s_1 mode, i.e.

$$\mathcal{P}_2'(x) = \mathrm{Re}(s_1)|B_1|^2 \int_0^1 |Y_1(y)|^2 \,\mathrm{d}y\, \mathrm{e}^{-2\,\mathrm{Im}(s_1)x}. \tag{4.7}$$

For figure 8*a*,*b*, it is clear that the total power transmitted along the duct is less attenuated than $\mathcal{P}_2'$, and this is due to the linear (EP2) and quadratic (EP3) terms in x present in the additional eigenfunctions of ψ_2 which reduce the attenuation. In fact, the power transmitted along the

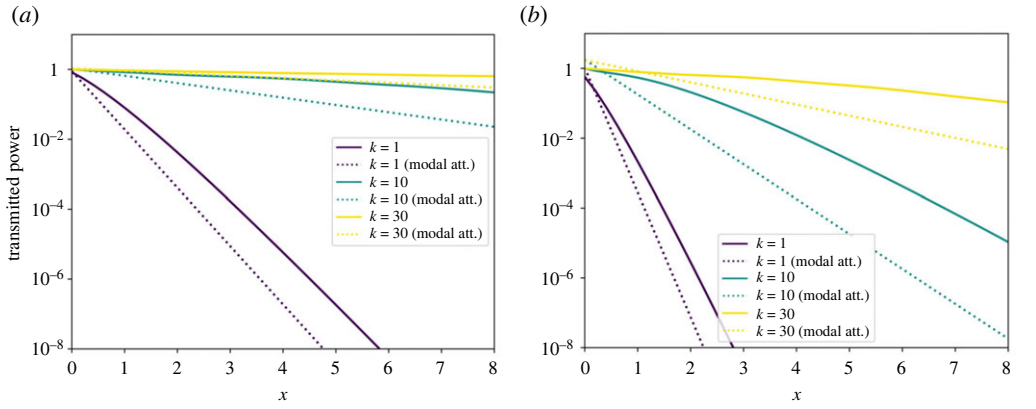

Figure 8. The transmitted power (logarithmic scale) against x for $k = 1, 10, 30$: (*a*) at the first Tester EP2 and (*b*) at the first EP3 with absorbing walls. Solid lines correspond to the numerical solution, computed with $N = 60$ modes, and dotted lines show power associated with the usual separable s_1 mode, i.e. $\mathcal{P}_2'(x)$. (Online version in colour.)

waveguide is dominated by those terms (two for EP2 and three for EP3) with wavenumber s_1; the reader is reminded that this is the least attenuated wavenumber. It is easy to show that

$$\mathrm{Im}(s_1) \approx \begin{cases} \mathrm{Re}(\alpha_1)\left(1 - \frac{k^2}{2|\alpha_1|^2}\right), & k \ll |\alpha_1| \\ -\frac{\mathrm{Re}(\alpha_1)\mathrm{Im}(\alpha_1)}{(2k)}, & k \gg |\alpha_1| \end{cases}, \tag{4.8}$$

so the attenuation of $\mathcal{P}_2'$ decreases as k increases,[3] which is confirmed by the dotted lines in figure 8*a*. As expected, the transmitted power for EP3, figure 8*b*, shows much stronger attenuation than the EP2 case, and this is consistent with the fact that for EP3 both the real and imaginary parts of α_1 are approximately twice those for EP2 (table 1). It is worthwhile noting that the higher order modes (s_n, $n > 1$) do not contribute significantly to the transmitted power for any of the frequencies considered herein. Thus, the only modal coefficients relevant to the transmitted power are B_1, $\bar{B}_1$ and, for EP3, $\bar{\bar{B}}_1$, although it is necessary to take many more modes in the mode-matching scheme to calculate these accurately.

In view of the high modal attenuation observed at EP3 [23], the behaviour of the TL close to EP3 shown in figure 3 and the plots of transmitted power shown in figure 8, it is tempting to imagine that EP3 may correspond to maximum TL for the problem under consideration. To explore this concept, the TL across the region of the $\bar{\alpha}$-plane corresponding to absorbing liners is considered. The wall parameters $\bar{\mu}$ and $\bar{\nu}$ are evaluated using (2.13), after which the enhanced EP2 matching is used to generate the solution. The results are mapped in figure 9 for $k = 1, 5, 10$ at $x = 1$ and $x = 10$ (the reflected power is also shown). It is clear from figure 9*c*,*f*,*i*, (corresponding to $x = 10$) that EP3 (denoted by a star) always lies in a zone corresponding to high TL but not necessarily the maximum TL (which is obtained in the yellow regions of the TL maps).

Figure 10 shows the magnitude of the potential for $-4 < x < 4$, $0 \le y \le 1$ at the first EP3 of table 1 for various values of k. When $k \ge 5$, a focal spot (where the magnitude of the potential ψ_2 is larger than that of ψ_1) can be observed. While not conflicting with energy conservation, this amplification does contradict the usual expectation that a dissipative system, with only exponentially decaying modes, leads to a monotonically decreasing field. The value of the x coordinate at which the spot appears will depend on the form of the incident field and the frequency. This is consistent with the observations of Makris *et al.* in the context of photonic media [24]. In that case, it was observed that even when all the eigenvalues are in the loss plane,

[3]For the results presented in §4b, the reader is advised that μ and ν are treated as *fixed* parameters. No allowance is made for Z_μ and Z_ν (see the text following (2.4) to vary with k).

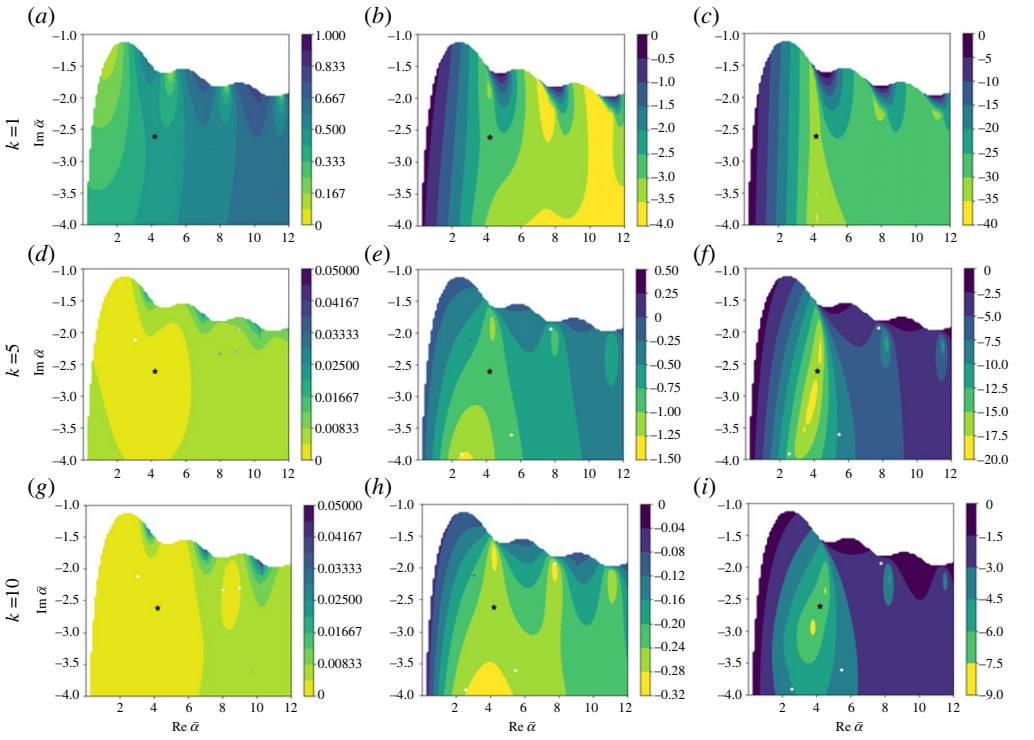

Figure 9. Reflected power, $\mathcal{R}$, (*a*, *d*, *g*), $\log_{10}\mathcal{T}(x=1)$ (*b*, *e*, *h*) and $\log_{10}\mathcal{T}(x=10)$ (*c*, *f*, *i*) for all passive $\bar{\mu}$ and $\bar{\nu}$ values that span the $\bar{\alpha}$ complex plane (based on equation (2.13)) at $k=1$ (*a*–*c*), $k=5$ (*d*–*f*) and $k=10$ (*g*–*i*). The star corresponds to EP3. (Online version in colour.)

the system may exhibit non-exponential transient behaviour (a focal point) before entering the exponential decay regime. A similar analysis has been presented in [19] for an acoustic waveguide with one lined wall. The latter authors show that for a carefully selected incident field (comprising a combination of modes), a transmitted power with almost no decay can be obtained in a transient region. This type of constructive interference is generally stronger at EP conditions because the additional waveforms introduce an element of growth in the x direction, again confirming the need for computational methods that are accurate at EPs.

The wall parameters used to generate figures 11–13 are those reported in the last line of table 1 for which one wall is passive and the other is active (the wall parameters forming a complex conjugate pair). It is worth noting that these parameters generate features that are common to PT-symmetric systems. However, the duct geometry considered here does not give rise to a fully PT symmetric system due to the lack of symmetry in x. To be precise, where the lined duct is of finite extent, it would generate a PT-symmetric system.[4] For this EP3, all the transverse wavenumbers (see 2.7) are real[5] (which is common in PT-symmetric systems). Further, due to the complex conjugate values of the wall parameters, the system has both loss and gain, however, (4.3) still applies. Since the axial wavenumbers are either real or purely evanescent, they produce no amplification. Thus, this configuration allows a direct observation of the quadratic nature of the additional waveforms. To illustrate this, figure 11*a* shows the power transmitted along the waveguide and figure 11*b* shows the potential ψ_2 on the midline $y=0.5$, here $k=5$ which is

[4]The PT symmetry in y arises because the wave equation and boundary conditions are invariant under the substitution $\tilde{y}$ to $-\tilde{y}$ (where $\tilde{y}=y-1/2$) together with taking the complex conjugate of the whole boundary problem.

[5]It was observed numerically that *all* α_n are real valued in this specific scenario, although the reader is advised that having $\mu=\nu^*$ is a necessary but not a sufficient condition to have a completely real spectra.

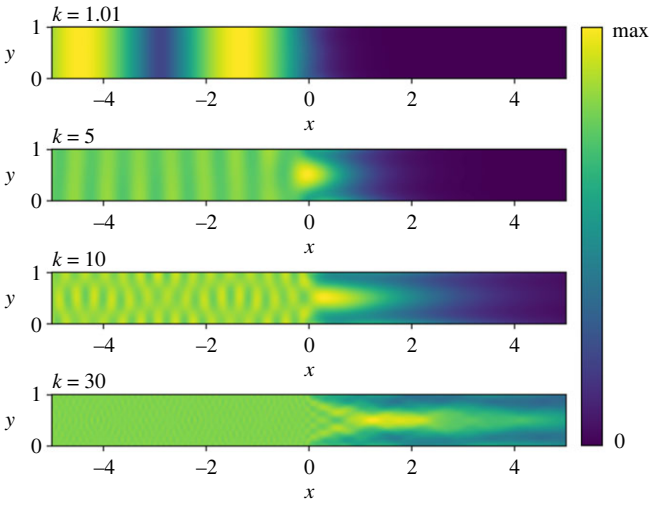

Figure 10. The magnitude of the potential field ($|\psi_1|$ for $x < 0$ and $|\psi_2|$ for $x > 0$) at the first EP3 (absorbing walls) of table 1, computed for different frequency values. The colour scale ranges from 0 to the max of each field. Note the focal spot occurring for $k \geq 5$. (Online version in colour.)

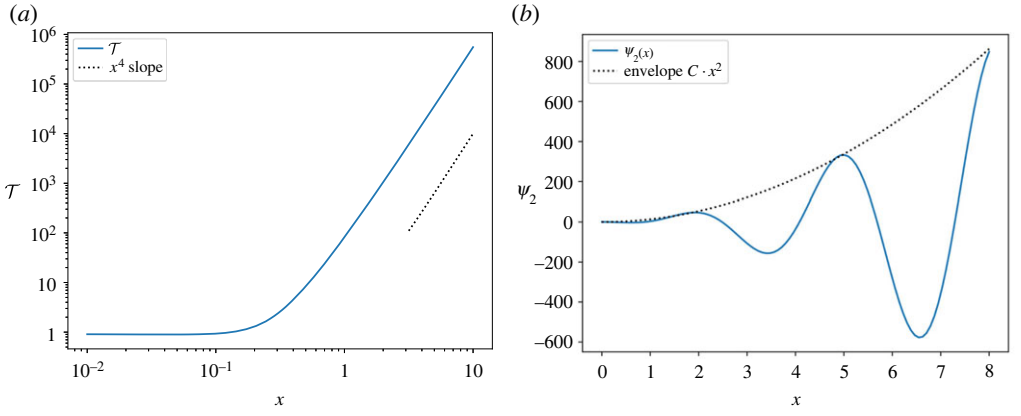

Figure 11. (*a*) Evolution of the transmitted power along the waveguide (logarithmic scales) and (*b*) the magnitude (envelope) and real part of the potential $\psi_2(x, 0.5)$ at $k = 5$ for the EP3-PT (one passive and one active wall) parameters. (Online version in colour.)

slightly above the lined duct cut-off. The quadratic growth of the envelope (typical of a beating phenomenon) is apparent and arises because $\alpha_1 \approx 4.6015$ is real. Beyond a transition zone near the matching interface, the transmitted power grows as $\mathcal{T} \sim x^4$ as expected from the additional waveforms.

The reflected power is displayed in figure 12. Below the cut-off for the inlet waveguide ($k \leq \pi$), results indicate perfect reflection, i.e. $\mathcal{R} = 1$. It is worth noting that waves cannot propagate in the lined duct below its cut-off, i.e. $k \leq 4.6015$, whereas when $k > 4.6015$ waves are able to propagate downstream ($x > 0$) unattenuated with real axial wavenumber(s). The reflected mode that cuts on when $k = \pi$ is anti-symmetric about $y = 1/2$, and it is interesting to note that for $\pi < k < 4.6015$ the reflected power is much greater than 1. Initial investigations into the acoustic intensity show that power is absorbed at the point $x = 0^+, y = 1$ and generated at $x = 0^+, y = 0$. The reader is reminded that the velocity field contains a logarithmic singularity and that the local re-construction of the

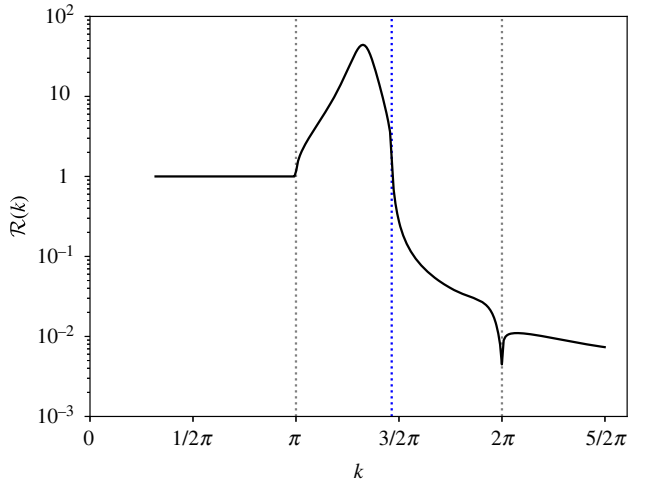

Figure 12. Reflected power (logarithmic scale) at EP3-PT (one passive and one active wall) against frequency k. (Online version in colour.)

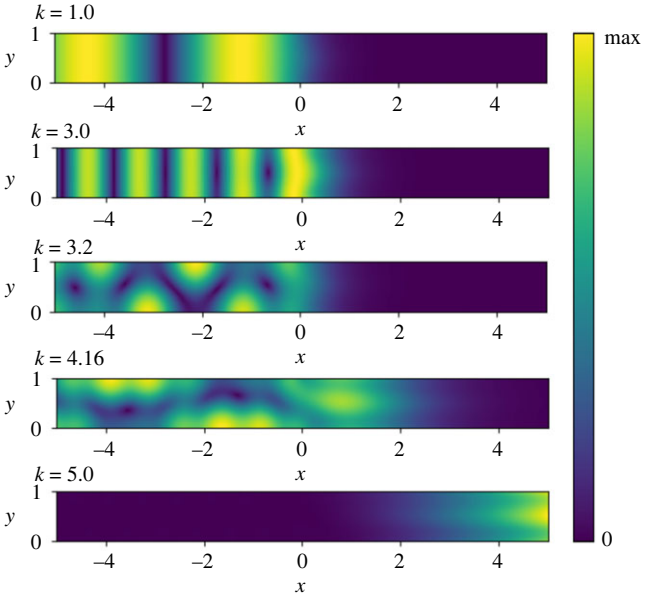

Figure 13. The magnitude of the potential field ($|\psi_1|$ for $x < 0$ and $|\psi_2|$ for $x > 0$) at EP3-PT (one passive and one active wall), computed at different frequency values. The colour scale ranges from 0 to the max of each field. (Online version in colour.)

velocity field (i.e. close to $x = 0$) is affected by the Gibb's phenomenon, so caution is needed in interpreting this result. However, it would appear that the energy generated at $x = 0^+, y = 0$ is reflected because it cannot be transmitted at this frequency. The maximal value of the reflected power is reached when $k \approx 4.18$ and, interestingly, the determinant of the matching matrix vanishes close to $k = 4.18 \pm 0.21i$, which suggests the presence of a complex resonance. Figure 13 shows the magnitude of the potential for $-4 < x < 4$, $0 \leq y \leq 1$ for various values of k which have been specifically chosen to be below both cut-offs ($k = 1, 3$), between cut-offs ($k = 3.2, 4.16$) and above the lined duct cut-off ($k = 5$). For $k = 1, 3$, the potential is zero for $x > 0$ which is consistent

with total reflection. For $k = 4.16$ (which is close to the maximal reflected power), the potential is non-zero within a confined region, $0 < x < 2$, but zero beyond this. For $k = 5$, the potential is non-zero for $x > 0$ and increases with increasing x (as shown in figure 11).

5. Discussion

In this article, an enhanced mode-matching procedure, suitable for use in waveguides at EP conditions, has been presented and applied to a canonical model problem. The reader is reminded that, at an EP, the existence of additional non-separable waveforms is manifest by the self-orthogonality of one of the usual separable modes. This, in turn, leads to degeneracy of the standard mode-matching method close to and at EP conditions. The enhanced procedure regularizes this by incorporating the additional waveforms into the relevant modal expansion(s). The integrity of the enhanced mode-matching procedure has been explored. It has been shown that: for EP2, the enhanced modal expansion converges point-wise to the required function; the transmission loss is a continuous function of the wavenumber at both EP2 and EP3 (but that the standard method fails when implemented within 10^{-5} of the EP value of k); the mode-matching conditions are well satisfied at EP3; the condition number for the underlying algebraic system is always less than 50 for the enhanced procedure, but the standard procedure is ill conditioned when implemented in the vicinity of an EP.

Having established the integrity of the enhanced mode matching, the method was implemented to explore the reflected and transmitted power fields for various EP situations. The transmission loss (TL) was mapped (figure 9) for the region of the $\bar{\alpha}$-plane corresponding to absorbing liners. This reveals that, although it is broadly accepted that the best possible axial attenuation is achieved through the coalescence of the first three standard duct modes, EP3 does not necessarily correspond to maximum TL. It is clear that EP3 does produce very good TL, but there are small areas of the map (shown in yellow) where the TL is better. Further, EP3 generates some interesting and unusual phenomena. On mapping the magnitude of the velocity potential for the absorbing EP3 of table 1 within the duct for $-4 < x < 4$, $0 \leq y \leq 1$, a focal spot is observed for $x > 0$. At this point, the magnitude of the transmitted field is larger than the amplitude of the incident field. Such behaviour is unusual for a dissipative system and occurs here due to the quadratic x-dependence of the non-separable waveforms that are unique to EP3. Beyond the focal spot, the field rapidly decays with increasing x. For the second EP3 of table 1, the wall parameters are such that $\mu = \nu^*$ and were the duct geometry to be symmetric in x (such that the lined duct was of finite length), the system would be PT symmetric. As it is, the system is not PT symmetric, but some interesting features can be observed in figures 11–13. It is worth noting that the far-field within the duct cannot be correctly calculated using standard mode-matching close to EP3. The enhanced matching, however, produces accurate results because the x-dependence of the envelope is built in through the additional, non-separable waveforms for EP3.

Finally, although the enhanced mode-matching method presented herein has been developed for a lined duct, it is worth noting that the additional waveforms, upon which the method depends, comprise derivatives of the standard separable waveforms with respect to the continuous axial wavenumber s [20,23]. It is, therefore, anticipated that the method will be easily extended to other classes of waveguide and provide a rigorous tool by which to study the effects of EPs in these systems.

Data accessibility. The paper contains no experimental data. All codes repositories address are available from the reference section.

Authors' contributions. J.B.L.: conceptualization, formal analysis, investigation, methodology and writing—original draft; B.N.: investigation, software, validation, visualization and writing—review and editing; E.P-D.: conceptualization, investigation, validation and writing—review and editing.

All authors gave final approval for publication and agreed to be held accountable for the work performed therein.

Conflict of interest declaration. We declare we have no competing interests.

Funding. No funding has been received for this article.

Appendix A. Orthogonality and point-wise convergence

(a) Orthogonality

In the absence of an EP, the travelling waveforms for the section of the duct lying in $x > 0$ (see §2) are separable in form and are defined as $Y(s, y)\,\mathrm{e}^{\mathrm{i}sx}$, where $Y(s, y)$ satisfies the eigensystem:

$$\partial_{yy}Y + \alpha^2 Y = 0, \quad \alpha = (k^2 - s^2)^{1/2},\ 0 \le y \le 1 \tag{A 1}$$

together with:

$$\partial_y Y = -\mu Y \quad \text{at } y = 0 \quad \text{and} \quad \partial_y Y = \nu Y \quad \text{at } y = 1. \tag{A 2}$$

Here, Y is a function of both s and y, and $Y(s_n, y) = Y_n(y)$, where s_n is an axial wavenumber. This eigen-system differs from a standard Sturm–Liouville system only in that the parameters μ and ν are complex.[6] On using the boundary conditions, it is clear that:

$$0 = \Big[(\partial_y Y_n - \nu Y_n)(\partial_y Y_m + \mu Y_m) - (\partial_y Y_m - \nu Y_m)(\partial_y Y_n + \mu Y_n)\Big]_0^1, \tag{A 3}$$

$$= (\nu + \mu)(s_n^2 - s_m^2)\int_0^1 Y_m Y_n \,\mathrm{d}y, \quad \nu \neq -\mu, \tag{A 4}$$

which demonstrate the orthogonality of Y_m and Y_n for $m \neq n$. Further, as $n \to m$,

$$\int_0^1 Y_m^2 \,\mathrm{d}y = \lim_{s_n \to s_m} \frac{[(\partial_y Y_n - \nu Y_n)(\partial_y Y_m + \mu Y_m) - (\partial_y Y_m - \nu Y_m)(\partial_y Y_n + \mu Y_n)]_0^1}{(\nu + \mu)(s_n^2 - s_m^2)} \tag{A 5}$$

$$= \lim_{s \to s_m} \frac{-K'(s)(\partial_y Y_m + \mu Y_m)_{y=1}}{2s(\nu + \mu)}$$

$$= -\frac{Y_m(1)}{2s_m} K'(s_m) = P_m, \tag{A 6}$$

where (A 5) has been simplified by noting that $K(s) = (\nu Y - \partial_y Y)_{y=1}$, see (2.6), and that

$$\partial_{s_n}(\partial_y Y_n + \mu Y_n)_{y=0} = 0,$$

the latter being true because, on differentiation with respect to s_n, all the terms are either odd in y or contain a multiplicative y and thus are zero when $y = 0$.

At EP2 the additional eigenfunction, $\chi(y)$, is needed to ensure that the set of eigenfunctions is complete. It is worth noting that, by construction, χ satisfies the same boundary conditions as $Y(s, y)$ but a different governing equation: $\chi_{yy} + \alpha_1^2 \chi = -2\alpha_1^2 Y_1$. The orthogonality relation (3.13) is derived as follows. On using the boundary conditions:

$$0 = [(\partial_y \chi - \nu\chi)(\partial_y Y_m + \mu Y_m) - (\partial_y Y_m - \nu Y_m)(\partial_y \chi + \mu\chi)]_0^1, \tag{A 7}$$

$$= -2\alpha_1^2(\nu + \mu)\int_0^1 Y_1 Y_m \,\mathrm{d}y + (\nu + \mu)(s_1^2 - s_m^2)\int_0^1 \chi Y_m \,\mathrm{d}y, \tag{A 8}$$

which (since $P_1 = 0$) confirms that χ is orthogonal to Y_m, $m \neq 1$. It also follows that

$$\int_0^1 \chi Y_1 \,\mathrm{d}y = \lim_{s_m \to s_1} \frac{[(\partial_y \chi - \nu\chi)(\partial_y Y_m + \mu Y_m) - (\partial_y Y_m - \nu Y_m)(\partial_y \chi + \mu\chi)]_0^1}{(\nu + \mu)(s_1^2 - s_m^2)}$$

$$+ \lim_{s_m \to s_1} \frac{2\alpha_1^2}{s_1^2 - s_m^2}\int_0^1 Y_1 Y_m \,\mathrm{d}y. \tag{A 9}$$

[6]The case corresponding to $\nu = -\mu$ is not included in the present analysis.

In this case, the first limit on the right-hand side of (A 9) is zero and the second can be evaluated using (A 5). Thus,

$$\int_0^1 \chi Y_1 \,\mathrm{d}y = 2\alpha_1^2 \lim_{m\to 1} \frac{[(\partial_y Y_1 - \nu Y_1)(\partial_y Y_m + \mu Y_m) - (\partial_y Y_m - \nu Y_m)(\partial_y Y_1 + \mu Y_1)]_0^1}{(\nu+\mu)(s_1^2 - s_m^2)^2}$$
$$= \frac{\alpha_1^2 Y_1(1)}{4s_1^2} K''(s_1) = Q. \tag{A 10}$$

At EP3, $P_1 = Q = 0$, and a further eigenfunction, $\xi(y)$, is required in addition to $\chi(y)$ in order that the set of eigenfunctions is complete. Again, it is worth noting that, by construction, $\xi(y)$ satisfies the same boundary conditions as $Y(s,y)$ but, in this case, $\xi_{yy} + \alpha_1^2 \xi = 2Y_1 + 4\chi$. The orthogonality relation (3.23) is derived using the analogous process as that for χ but, for the sake of brevity, the details are omitted. The reader is also advised that the same method can be used to evaluate T, and the result is included here for use in the next section. The algebra is not for the faint hearted, but it can be shown that:

$$T = \int_0^1 \chi^2(y)\,\mathrm{d}y = Q\left(\frac{\alpha_1^2}{s_1^2} + \nu + \frac{\mu(\mu-\nu)}{\alpha_1^2+\mu^2}\right) - \frac{\alpha_1^2}{2} R. \tag{A 11}$$

(b) Point-wise convergence at EP2

In the absence of an EP, the set of eigenfunctions $Y_n(y)$, $n = 1, 2, 3, \ldots$ are complete, and point-wise convergence of the modal expansions to the functions ψ_j, $j = 1, 2$ (and their x derivatives) is assured. However, at EP2, $Y_1(y)$ is self-orthogonal and another function must be added to the set to ensure point-wise convergence. In §3, the function $\chi(y)$ was introduced, and here, it is proved that this is an appropriate choice. For the sake of brevity, only the main steps of the method are presented, and the reader is referred to [32] for further details. Consider the integral

$$J_1(v,y) = \frac{1}{2\pi i} \int_{-\infty}^{\infty} \frac{sI(s,v)Y(s,y)}{K(s)Y(s,1)} \,\mathrm{d}s = 0, \quad 0 \le v, y \le 1, \tag{A 12}$$

where the integrand is odd, the path of integration is indented below (above) any poles on the negative (positive) real axis and

$$I(s,v) = \frac{1}{\alpha}\sin(\alpha v) + \frac{\mu}{\alpha^2}\cos(\alpha v). \tag{A 13}$$

Note that as $|s| \to \infty$, the integrand is $O(1/s)$ when $y = v = 1$ and is $o(1/s)$ otherwise, and that:

$$\frac{\mathrm{d}I}{\mathrm{d}v}(s,v) = Y(s,v). \tag{A 14}$$

The integrand contains two families of poles, corresponding to $K(s) = 0$ and $Y(s,1) = 0$, and a pole at $\alpha = 0$. In the case of no EP, on closing the path of integration in the upper half plane and summing the residues, it is found that

$$\sum_{n=1}^{\infty} \frac{I(s_n,v)Y_n(y)}{P_n} = 2\sum_{n=1}^{\infty} \frac{\delta_n I(\delta_n,v)Y(\delta_n,y)}{K(\delta_n)Y'(\delta_n,1)}$$
$$- \frac{\mu(1-\mu y)}{(1-\mu)(\nu+\mu-\nu\mu)} + 2H(y+v-2), \tag{A 15}$$

where δ_n, $n = 1, 2, 3, \ldots$ are the roots of $Y(s,1) = 0$ and $H()$ is the Heaviside function defined with $H(0) = 1/2$. On noting that $K(\delta_n) = \{\alpha(\delta_n) + \mu^2/\alpha(\delta_n)\}\sin[\alpha(\delta_n)]$, it becomes apparent that the sum

on the right-hand side can be evaluated by consideration of the integral:

$$J_2(v,y)=\frac{1}{2\pi i}\int_{-\infty}^{\infty}\frac{s\alpha I(s,v)Y(s,y)}{(\alpha^2+\mu^2)\sin(\alpha)Y(s,1)}\,\mathrm{d}s=0,\quad 0\le v,y<1. \tag{A 16}$$

On closing the path of integration in the upper half plane and summing the residues, it is found (after some algebraic manipulation) that

$$\begin{aligned}2\sum_{n=1}^{\infty}\frac{\delta_n I(\delta_n,v)Y(\delta_n,y)}{K(\delta_n)Y'(\delta_n,1)}&=-\frac{2}{\pi}\sum_{n=1}^{\infty}\frac{\sin(n\pi y)\cos(n\pi v)}{n}+\frac{(1-y)}{(1-\mu)}\\&=\frac{\mu(1-y)}{1-\mu}+H(-y-v)+H(v-y)-H(y+v-2).\end{aligned} \tag{A 17}$$

Expression (A 17) is valid for $0\le v,y\le 1$ with the exception of the isolated point $v=y=0$. Thus, on substituting (A 17) into (A 15) and differentiating with respect to v,

$$\sum_{n=1}^{\infty}\frac{Y_n(v)Y_n(y)}{P_n}=\delta(v-y)-\delta(v+y)+\delta(y+v-2),\quad 0<v,y\le 1, \tag{A 18}$$

where $\delta()$ is the Dirac delta function. This result confirms point-wise convergence in the case of no EP. At EP2, the result is altered slightly due to the presence of a double pole in the integrand of (A 12). As in the main body of the article, attention will be restricted to the case where the EP occurs at $s=s_1$. The appropriate result becomes

$$\sum_{n=2}^{\infty}\frac{Y_n(v)Y_n(y)}{P_n}-2\partial_v\rho(v,y)|_{s=s_1}=\delta(v-y)-\delta(v+y)+\delta(y+v-2), \tag{A 19}$$

where $0<v,y\le 1$ and $-\rho(v,y)$ is the residue contribution due to the double pole in the integrand of (A 12). It is found that

$$\partial_v\rho(v,y)|_{s=s_1}=\lim_{s\to s_1}\frac{\mathrm{d}}{\mathrm{d}s}\left\{\frac{(s-s_1)^2sY(s,v)Y(s,y)}{K(s)Y(s,1)}\right\}, \tag{A 20}$$

$$\begin{aligned}&=\frac{2s_1}{K''(s_1)Y_1(1)}\left\{\frac{1}{s_1}-\frac{Y'(s,1)|_{s=s_1}}{Y_1(1)}-\frac{K'''(s_1)}{3K''(s_1)}\right\}Y_1(v)Y_1(y)\\&\quad+\frac{2s_1}{K''(s_1)Y_1(1)}\{Y'(s_1,v)Y_1(y)+Y_1(v)Y'(s_1,y)\},\end{aligned} \tag{A 21}$$

where, as usual, the prime indicates differentiation with respect to s. On using (3.10) and after some manipulation,

$$\begin{aligned}\partial_v\rho(v,y)|_{s=s_1}&=\frac{2s_1}{K''(s_1)Y_1(1)}\left\{\frac{1}{s_1}-\frac{K'''(s_1)}{3K''(s_1)}+\frac{s_1v}{\alpha_1^2}+\frac{s_1\mu(\mu-v)}{\alpha_1^2(\alpha_1^2+\mu^2)}\right\}Y_1(v)Y_1(y)\\&\quad-\frac{1}{2Q}\{\chi(v)Y_1(y)+Y_1(v)\chi(y)\},\end{aligned} \tag{A 22}$$

from which, using (A 11), it follows that

$$\begin{aligned}&\sum_{n=2}^{\infty}\frac{Y_n(v)Y_n(y)}{P_n}+\frac{\chi(v)Y_1(y)+Y_1(v)\chi(y)}{Q}-\frac{T}{Q^2}Y_1(v)Y_1(y)\\&\quad=\delta(v-y)-\delta(v+y)+\delta(y+v-2),\quad 0<v,y\le 1.\end{aligned} \tag{A 23}$$

Point-wise convergence in the case of EP2 can now be demonstrated by multiplying (A 23) by an arbitrary, suitably smooth function $g(v)$, $v\in(0,1)$ and integrating across $0\le v\le 1$. It is found that

$$g(y)=\sum_{n=2}^{\infty}\frac{C_n}{P_n}Y_n(y)+\left(\frac{\bar{C}_1}{Q}-\frac{TC_1}{Q^2}\right)Y_1(y)+\frac{C_1}{Q}\chi(y), \tag{A 24}$$

where the generalized Fourier coefficients are given by:

$$\bar{C}_1 = \int_0^1 g(v)\chi(v)\,\mathrm{d}v \quad \text{and} \quad C_n = \int_0^1 g(v)Y_n(v)\,\mathrm{d}v, \quad n \geq 1.$$

Thus, at EP2, an arbitrary smooth function, $g(y)$, $y \in (0,1)$, can be expressed as a generalized Fourier series in terms of $\chi(y)$ and $Y_n(y)$, $n = 1, 2, 3, \ldots$.

It is worth noting that the same method could be used to prove point-wise convergence in the case of EP3; however, the algebra is anticipated to be somewhat more complicated. Instead, as a means of validating the use of ξ and χ in the mode-matching method at EP3, it is demonstrated numerically that the matching conditions for the problem considered in the main body of the article are satisfied in this case, see figure 5.

References

1. Cremer L. 1953 Theory of sound attenuation in a rectangular duct with an absorbing wall and the resultant maximum attenuation coefficient. *Acustica* **2**, 249–263.
2. Krasnok A, Baranov D, Li H, Miri M-A, Monticone F, Alú A. 2019 Anomalies in light scattering. *Adv. Opt. Photonics* **11**, 892–951. (doi:10.1364/AOP.11.000892)
3. Ashida Y, Gong Z, Ueda M. 2020 Non-hermitian physics. *Adv. Phys.* **69**, 249–435. (doi:10.1080/00018732.2021.1876991)
4. Miri M-A, Alu A. 2019 Exceptional points in optics and photonics. *Science* **363**, eaar7709. (doi:10.1126/science.aar7709)
5. Tester BJ. 1973 The optimization of modal sound attenuation in duct, in the absence of mean flow. *J. Sound Vib.* **27**, 477–513. (doi:10.1016/S0022-460X(73)80358-X)
6. Zorumski WE, Mason JP. 1974 Multiple eigenvalues of sound-absorbing circular and annular ducts. *J. Acoust. Soc. Am.* **55**, 1158–1165. (doi:10.1121/1.1914680)
7. Koch W. 1977 Attenuation of sound in multi-element acoustically lined rectangular ducts in the absence of mean flow. *J. Sound Vib.* **52**, 459–496. (doi:10.1016/0022-460X(77)90365-0)
8. Kabral R, Du L, Åbom M. 2016 Optimum sound attenuation in flow ducts based on the on the exact Cremer impedance. *Acta Acust. United Acust.* **102**, 851–860. (doi:10.3813/AAA.918999)
9. Qiu X, Du L, Jing X, Sun X. 2019 The Cremer concept for annular ducts for optimum sound attenuation. *J. Sound Vib.* **438**, 383–401. (doi:10.1016/j.jsv.2018.09.029)
10. Zhang Z, Bodén H, Åbom M. 2019 The Cremer impedance: an investigation of the low frequency behavior. *J. Sound Vib.* **459**, 114844. (doi:10.1016/j.jsv.2019.07.010)
11. Xiong L, Nennig B, Aurégan Y, Bi W. 2017 Sound attenuation optimization using metaporous materials tuned on exceptional points. *J. Acoust. Soc. Am.* **142**, 2288–2297. (doi:10.1121/1.5007851)
12. Spillere A, Cordioli JA. 2019 Optimum acoustic impedance in circular ducts with inviscid sheared flow: application to turbofan engine intake. *J. Sound Vib.* **443**, 502–519. (doi:10.1016/j.jsv.2018.12.007)
13. Sánchez JR, Piot E, Casalis G. 2012 Theoretical and numerical investigation of optimal impedance in lined ducts with flow. In *Acoustics 2012, Nantes, France, 23–27 April 2012*, pp. 3437–3442.
14. Goldzak T, Mailybaev AA, Moiseyev N. 2018 Light stops at exceptional points. *Phys. Rev. Lett.* **120**, 013901. (doi:10.1103/PhysRevLett.120.013901)
15. Orchini A, Magri L, Silva CF, Mensah GA, Moeck JP. 2020 Degenerate perturbation theory in thermoacoustics: high-order sensitivities and exceptional points. *J. Fluid Mech.* **903**, A37. (doi:10.1017/jfm.2020.586)
16. Feng L, Zhu X, Yang S, Zhu H, Zhang P, Yin X, Wang Y, Zhang X. 2014 Demonstration of a large-scale optical exceptional point structure. *Opt. Express* **22**, 1760–1767. (doi:10.1364/OE.22.001760)
17. Bi W, Pagneux V. 2015 New insights into mode behaviours in waveguides with impedance boundary conditions. Preprint (https://arxiv.org/abs/1511.05508).
18. Kelsten M. 2018 Modeling of acoustic waves in pipes with impedance walls and double roots. PhD thesis. New Brunswick, NJ: Rutgers University-School of Graduate Studies.
19. Guo W, Liu J, Bi W, Yang D, Aurégan Y, Pagneux V. 2020 Spatial transient behavior in waveguides with lossy impedance boundary conditions. Preprint (https://arxiv.org/abs/2010.03646).

20. Shenderov EL. 2000 Helmholtz equation solutions corresponding to multiple roots of the dispersion equation for a waveguide with impedance walls. *Acoust. Phys.* **46**, 357–363. (doi:10.1134/1.29892)
21. Longhi S. 2010 Spectral singularities and Bragg scattering in complex crystals. *Phys. Rev. A* **81**, 022102. (doi:10.1103/PhysRevA.81.022102)
22. Graefe E-M, Jones HF. 2011 PT-symmetric sinusoidal optical lattices at the symmetry-breaking threshold. *Phys. Rev. A* **84**, 013818. (doi:10.1103/PhysRevA.84.013818)
23. Perrey-Debain E, Nennig B, Lawrie JB. 2021 Mode coalescence and the Green's function in a two-dimensional waveguide with arbitrary admittance boundary conditions. *J. Sound Vib.* **516**, 116510. (doi:10.1016/j.jsv.2021.116510)
24. Makris KG, Ge L, Türeci HE. 2014 Anomalous transient amplification of waves in non-normal photonic media. *Phys. Rev. X* **4**, 041044. (doi:10.1103/PhysRevX.4.041044)
25. Nennig B, Perrey-Debain E. 2020 A high order continuation method to locate exceptional points and to compute puiseux series with applications to acoustic waveguides. *J. Comp. Phys.* **412**, 109425. (doi:10.1016/j.jcp.2020.109425)
26. Midya B, Konotop VV. 2016 Modes and exceptional points in waveguides with impedance boundary conditions. *Opt. Lett.* **41**, 4621–4624. (doi:10.1364/OL.41.004621)
27. Ge L, Makris KG, Christodoulides DN, Feng L. 2015 Scattering in PT- and RT-symmetric multimode waveguides: generalized conservation laws and spontaneous symmetry breaking beyond one dimension. *Phys. Rev. A* **92**, 062135. (doi:10.1103/PhysRevA.92.062135)
28. Bender CM. 2018 *PT symmetry: in quantum and classical physics*. Singapore: World Scientific Publishing.
29. Özdemir ŞK, Rotter S, Nori F, Yang L. 2019 Parity–time symmetry and exceptional points in photonics. *Nat. Mater.* **18**, 783–798. (doi:10.1038/s41563-019-0304-9)
30. Nawaz R, Lawrie JB. 2013 Scattering of a fluid-structure coupled wave at a flanged junction between two flexible waveguides. *J. Acoust. Soc. Am.* **134**, 1939–1949. (doi:10.1121/1.4817891)
31. Lawrie JB, Afzal M. 2017 Acoustic scattering in a waveguide with a height discontinuity bridged by a membrane: a tailored Galerkin approach. *J. Eng. Math.* **105**, 99–115. (doi:10.1007/s10665-016-9885-3)
32. Lawrie JB. 2007 On eigenfunction expansions associated with wave propagation along ducts with wave-bearing boundaries. *IMA J. Appl. Math.* **72**, 376–394. (doi:10.1093/imamat/hxm004)
33. Lawrie JB. 2012 On acoustic propagation in three-dimensional rectangular ducts with flexible walls and porous linings. *J. Acoust. Soc. Am.* **131**, 1890–1901. (doi:10.1121/1.3683256)
34. Norris AN, Osipov AV. 1999 Far-field analysis of the Malyuzhinets solution for plane and surface waves diffraction by an impedance wedge. *Wave Motion* **30**, 69–89. (doi:10.1016/S0165-2125(98)00049-3)
35. Nennig B. 2021 Polze—a package to locate poles and zeros of a meromorphic function with their multiplicities. See https://github.com/nennigb/polze.
36. Kravanja P, Van Barel M, Haegemans A. 1999 On computing zeros and poles of meromorphic functions. In *Computational Methods And Function Theory 1997 - Proceedings Of The Third CMFT Conference* (eds N Papamichael, S Ruscheweyh, EB Saff), pp. 359–369. Singapore: World Scientific.
37. Nennig B. 2021 Matchingep—a python package for extending mode matching method on 2D waveguide tuned at an exceptional point. See https://github.com/nennigb/matchingep.
38. Lee SW, Jones WR, Campbell JJ. 1971 Convergence of numerical solutions of iris-type discontinuity problems. *IEEE Trans. Microw. Theory Techn.* **19**, 528–536. (doi:10.1109/TMTT.1971.1127569)
39. Maurel A, Mercier J-F, Félix S. 2014 Propagation in waveguides with varying cross section and curvature: a new light on the role of supplementary modes in multi-modal methods. *Proc. R. Soc. A* **470**, 20140008. (doi:10.1098/rspa.2014.0008)
40. Félix S, Maurel A, Mercier J-F. 2015 Improved multimodal methods for the acoustic propagation in waveguides with finite wall impedance. *Wave Motion* **54**, 1–10. (doi:10.1016/j.wavemoti.2014.11.007)
41. Nennig B, Perrey-Debain E, Ben Tahar M. 2010 A mode matching method for modeling dissipative silencers lined with poroelastic materials and containing mean flow. *J. Acoust. Soc. Am.* **128**, 3308–3320. (doi:10.1121/1.3506346)